


 Cite this: *RSC Adv.*, 2021, **11**, 10300

Fabrication of $\text{TiO}_2/\text{Fe}_2\text{O}_3/\text{CdS}$ systems: effects of Fe_2O_3 and CdS content on superior photocatalytic activity

 Hui Feng, ^{*a} Siqi Feng, ^b Niu Tang, ^c Songbai Zhang, ^d Xiangyang Zhang ^d and Bo Liu ^d

A heterostructured material of CdS and Fe_2O_3 nanoparticle-modified TiO_2 nanotube array (NTA) photoelectrode ($\text{TiO}_2/\text{Fe}_2\text{O}_3/\text{CdS}$) is reported in this work. $\text{TiO}_2/\text{Fe}_2\text{O}_3$ was prepared by annealing TiO_2 NTAs pre-loaded with Fe(OH)_3 , which was uniformly clung to TiO_2 NTAs using sequential chemical bath deposition (S-CBD). Subsequently, CdS nanoparticles were deposited on $\text{TiO}_2/\text{Fe}_2\text{O}_3$ using the successive ion layer adsorption and reaction (SILAR) technique. Three-dimensional (3D) $\text{TiO}_2/\text{Fe}_2\text{O}_3/\text{CdS}$ samples generated a photocurrent of approximately 4.92 mA cm^{-2} , with a photoconversion efficiency of 4.36%, which is more than 20 times higher than that of bare TiO_2 NTAs (0.22%) and 6 times that of $\text{TiO}_2/\text{Fe}_2\text{O}_3$ (0.71%). The photocatalytic activity was evaluated by the degradation of *p*-nitrophenol (PNP) under visible light ($\lambda > 420 \text{ nm}$). The $\text{TiO}_2/\text{Fe}_2\text{O}_3/\text{CdS}$ exhibited the best photocatalytic activity among all samples. Almost all PNP was degraded by $\text{TiO}_2/\text{Fe}_2\text{O}_3/\text{CdS}$ within 120 min. The enhancement of photocatalytic activity could be attributed to the promoted photo-induced electron and hole separation and migration on the basis of photoluminescence spectra, photocurrent measurements, and open-circuit photovoltage responses. In addition, the newly synthesized $\text{TiO}_2/\text{Fe}_2\text{O}_3/\text{CdS}$ can maintain high photocatalytic efficiency for five reuse cycles. Our findings provide a new idea for the low cost synthesis of high performance photocatalysts for the photodegradation of organic pollutants in aqueous solution.

 Received 9th January 2021
 Accepted 23rd February 2021

 DOI: 10.1039/d1ra00195g
rsc.li/rsc-advances

1. Introduction

TiO_2 is very attractive due to its fascinating features such as plentiful polymorphs, good chemical and thermal stability, and excellent electronic and optical properties.¹ TiO_2 nanotubes have a larger specific surface area and exchange capacity, as well as higher surface energy and extremely strong adsorption capacity compared with other TiO_2 nanomaterials.^{2,3} Furthermore the conductive substrate of Ti is closely connected with the highly ordered porous nanotube, which accelerates the separation of photogenerated charges and inhibits their recombination, so the photoelectric efficiency is improved. However, TiO_2 is active only under near-ultraviolet irradiation, only around 4% of the incident solar spectrum energy, due to its wide band gap energy of 3.0–3.2 eV.^{4,5}

Numerous attempts were made to extend the light absorption of TiO_2 to the visible light range, which accounts for around

48% of the incident solar energy.⁶ Fe_2O_3 is considered to be one of the best co-catalyst candidates due to its appropriate band gap ($E_g \sim 2.2 \text{ eV}$) for solar light harvesting, good photochemical stability, earth abundance, nontoxicity and low cost.⁷ For example, Kuang *et al.*⁵ reported the fabrication, characterization and photoelectrochemical properties of Fe_2O_3 modified TiO_2 nanotube arrays. Moniz *et al.*⁸ demonstrated that the decoration of Fe_2O_3 nanoclusters on TiO_2 leads to better charge separation and enhanced photocatalytic activity. Xia *et al.*⁹ prepared novel $\alpha\text{-Fe}_2\text{O}_3@\text{TiO}_2$ core/shell nanocomposites with improved photocatalytic activity in the visible light region. X. Lv *et al.*³ designed $\text{Fe}_2\text{O}_3@\text{TiO}_2$ nanotube composite anodes for lithium-ion batteries. Sun *et al.*¹⁰ demonstrated the effect of surface Fe_2O_3 clusters on the photocatalytic activity of TiO_2 for phenol degradation in water. Yao *et al.*⁷ proved that Fe_2O_3 nanothorns sensitized two-dimensional TiO_2 nanosheets with highly efficient solar energy conversion. Cao *et al.*¹¹ synthesized $\text{Fe}_2\text{O}_3\text{-B-TiO}_2$ superstructures with highly promoted photocatalytic activity and recyclability.

Previous studies have shown that co-sensitizing TiO_2 with different nanocrystals such as $\text{CdS/ZnIn}_2\text{S}_4$,⁴ CdTe/Mn-CdS ,¹² $\text{CdS-Mn/MoS}_2/\text{CdTe}$,¹³ $\text{CdS/CuIn}_2\text{S}_2/\text{Au}$,¹⁴ Mn-CdS/MoS_2 ,¹⁵ and CdS-based photocatalysts^{16–18} can extend the light absorption to the infrared range, and more importantly align the energy bands of the semiconductor. In summary, combining TiO_2 with Fe_2O_3 and CdS semiconductors could largely improve the photocatalytic activity of the co-sensitized electrode, as the energy

^aChangsha Environmental Protection College, Changsha 410082, Hunan Province, China. E-mail: hufeng_saint2000@163.com

^bCollege of Environmental Engineering, Shandong Construction University, Jinan 250000, China

^cState Key Lab of Chemo/Biosensing & Chemometrics, College of Chemistry & Chemical Engineering, Hunan University, Changsha 410082, China

^dCollege of Chemistry and Materials Engineering, Hunan University of Arts and Science, Changde, Hunan Province 415000, China



levels of Fe_2O_3 (bandgap ~ 2.2 eV), CdS (~ 2.4 eV), and TiO_2 (3.0–3.2 eV) are well suitable to one another, which benefits the separation of e^- – h^+ pairs.¹⁵

Herein, we fabricated $\text{TiO}_2/\text{Fe}_2\text{O}_3/\text{CdS}$ ternary heterostructures using a facile S-CBD method coupled with SILAR (Fig. 1). So far, to our knowledge, Ruiyang Yin *et al.*¹⁹ demonstrated a $\text{CdS}/\alpha\text{-Fe}_2\text{O}_3/\text{TiO}_2$ nanorod array for efficient photoelectrochemical (PEC) water oxidation that exhibits an improved photocurrent density of 0.62 mA cm^{-2} , while the photocurrent density of the present work reaches 4.92 mA cm^{-2} with a 20 fold photoconversion efficiency increase compared to bare TiO_2 photoanodes.

2. Experimental

2.1. Materials and methods

Titanium foil (99.8%, 0.127 mm thick) was purchased from Aldrich (Milwaukee, WI). Other reagents were of analytical grade. Double distilled water was used throughout the experiments. Titanium foil was cut into $1.0 \text{ cm} \times 3.5 \text{ cm}$ strips. The strips were ultrasonically cleaned in acetone and ethanol each for 5 min, respectively. The cleaned titanium strips were anodized at a constant potential of 25 V in an electrolyte containing 0.1 M NaF and 0.5 M NaHSO_4 at room temperature for 3 h in a two electrode configuration with a platinum cathode and the Ti strip as the anode. After oxidation, the prepared TiO_2 NTAs by an anodic oxidation process were directly successively immersed in NaOH , H_2O , FeCl_3 , and H_2O for 5 min each. Fe(OH)_3 was then successfully deposited onto the TiO_2 NTAs by S-CBD.²⁰ The immersion cycle was repeated five times. The amount of loaded Fe(OH)_3 was controlled by varying the FeCl_3 concentration at 0.01, 0.02, 0.05, 0.08, 0.10, 0.20, and 0.30 M, respectively. The TiO_2 NTAs loaded with Fe(OH)_3 were annealed

for crystallization at 550°C for 4 h to obtain the Fe_2O_3 -modified TiO_2 NTA photocatalysts. Second, the synthetic $\text{TiO}_2/\text{Fe}_2\text{O}_3$ was successively immersed in two different solutions for 1 min each: first in ethanol solution, 0.05 mol L^{-1} $\text{Cd}(\text{NO}_3)_2$ as the cation source, and then in 0.05 mol L^{-1} Na_2S in methanol/water (7 : 3 v/v). Following each immersion, the composite was rinsed for 2 min or longer with pure ethanol and methanol, respectively, to remove excess precursors and dried before the next dipping.^{15,21} The loading amount of the deposit was controlled by adjusting the number of immersion cycles; here, 1, 3, 5, 7 and 9 cycles were chosen for deposition. After washing several times with distilled water, the resulting $\text{TiO}_2/\text{Fe}_2\text{O}_3/\text{CdS}$ heterostructure was heated under a nitrogen atmosphere at 300°C for 2 h.

2.2. Photoelectrochemical measurements and structural characterization

The photocurrent measurements were conducted on a CHI-660C electrochemical system (Shanghai Chenhua Instrument Co. Ltd., China) using a standard three electrode cell with a working electrode, a platinum wire counter electrode, and a saturated calomel electrode (SCE) reference electrode. A solution containing 1 M KOH was used as the electrolyte. The sample ($\text{TiO}_2/\text{Fe}_2\text{O}_3/\text{CdS}$) was applied as the working electrode.²² A Xe lamp (CHF-XQ-500W, Beijing Changtuo Co. Ltd.) served as the light source. The incident light was filtered to match the AM 1.5G spectrum with an intensity of 100 mW cm^{-2} as measured with a radiometer (OPHIR, Littleton, CO). Scanning electron microscopy (SEM) images were recorded on a field-emission scanning electron microscope (SEM, JSM-6700F). Transmission electron microscopy (TEM) images and selected area electron diffraction (SAED) patterns were recorded on a JEOL JEM 2100 high resolution transmission electron

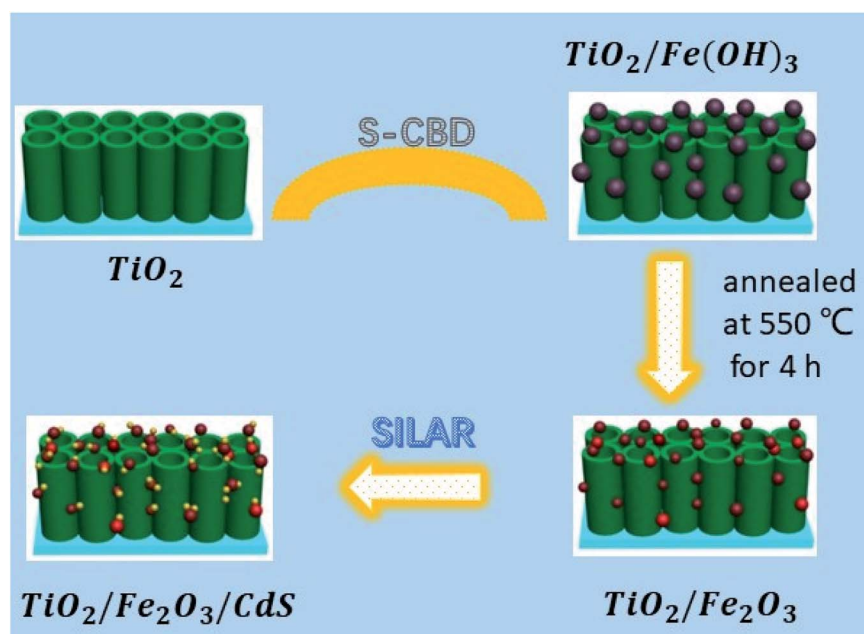


Fig. 1 Schematic illustration of the construction of $\text{TiO}_2/\text{Fe}_2\text{O}_3/\text{CdS}$ heterostructures.



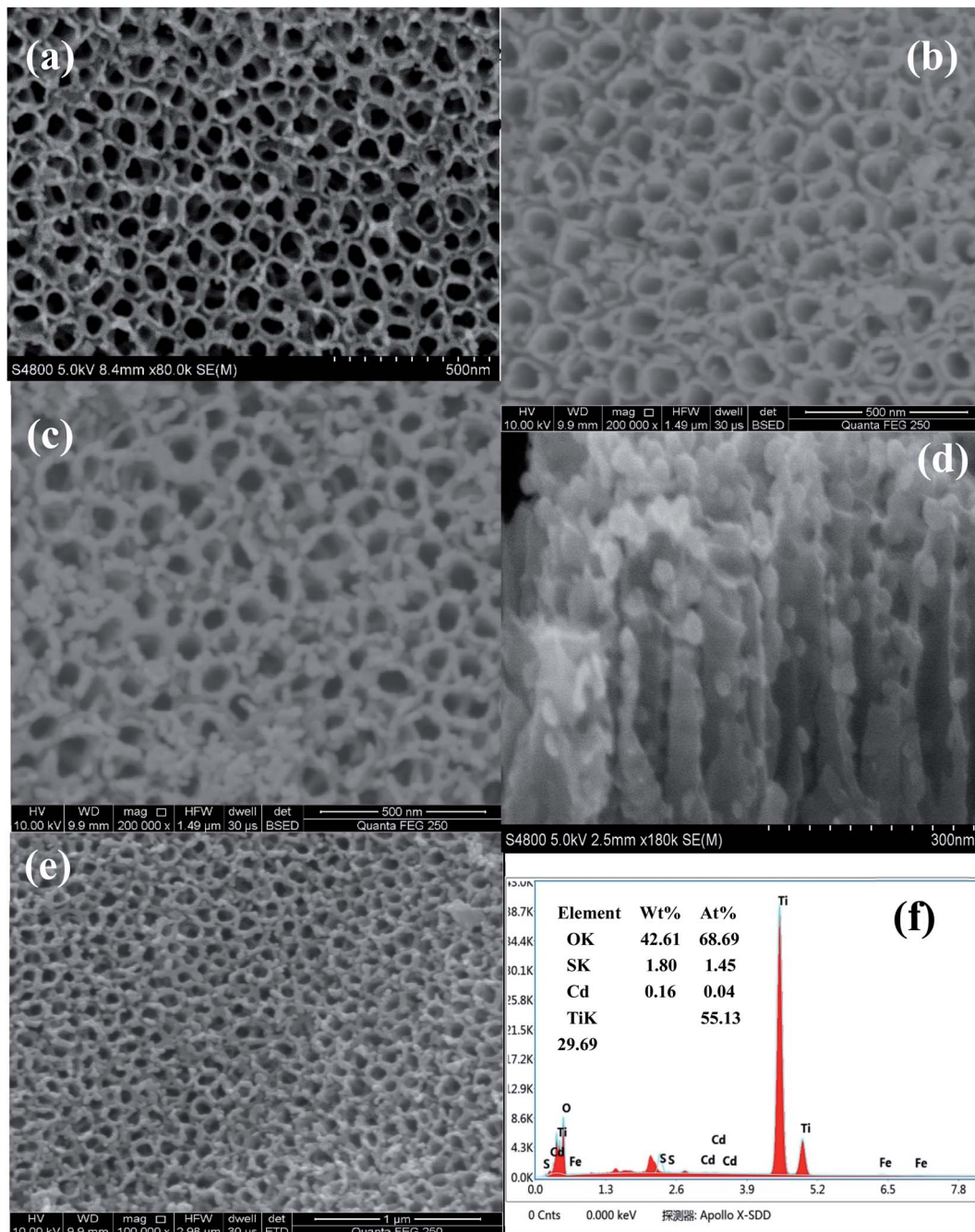


Fig. 2 SEM of TiO_2 nanotube arrays (a), top view of the $\text{TiO}_2/\text{Fe}_2\text{O}_3$ heterostructure (b) and $\text{TiO}_2/\text{Fe}_2\text{O}_3/\text{CdS}$ heterostructure (c), cross-sectional view of the $\text{TiO}_2/\text{Fe}_2\text{O}_3/\text{CdS}$ heterostructure (d), SEM images of the $\text{TiO}_2/\text{Fe}_2\text{O}_3/\text{CdS}$ heterostructure under different magnification (e), and the corresponding EDS of the $\text{TiO}_2/\text{Fe}_2\text{O}_3/\text{CdS}$ heterostructure (f).

microscope. An energy dispersive X-ray (EDX) spectrometer fitted to an electron microscope was used for elemental analysis. X-ray diffraction (XRD) patterns were recorded for identification of crystal structures of the samples with an X-ray diffractometer (XRD, M21X, MAC Science Ltd., Japan) employing $\text{Cu K}\alpha$ radiation ($\lambda = 1.54060 \text{ \AA}$). Light absorption properties were examined using UV-vis diffuse reflectance spectra (DRS, SHIMADZU, UV-2450) within a wavelength range of 200–800 nm. Photoluminescence (PL) spectra were recorded using a Hitachi F-4600 fluorescence spectrophotometer (Japan).

2.3. Photocatalytic degradation of PNP

The photocatalytic decomposition of PNP solution under visible light was performed to investigate the photocatalytic activities of $\text{TiO}_2/\text{Fe}_2\text{O}_3$ and $\text{TiO}_2/\text{Fe}_2\text{O}_3/\text{CdS}$ in comparison with those of the pure TiO_2 NTAs. For the test, the incident light intensity was adjusted to 100 mW cm^{-2} through an IR cut filter ($\lambda \geq 800 \text{ nm}$) and a UV cut filter ($\lambda < 400 \text{ nm}$) from a 500 W Xe lamp. The PNP solution (0.1 L , 20 mg L^{-1}) was illuminated for 2 h under magnetic stirring. The characteristic absorption of PNP at

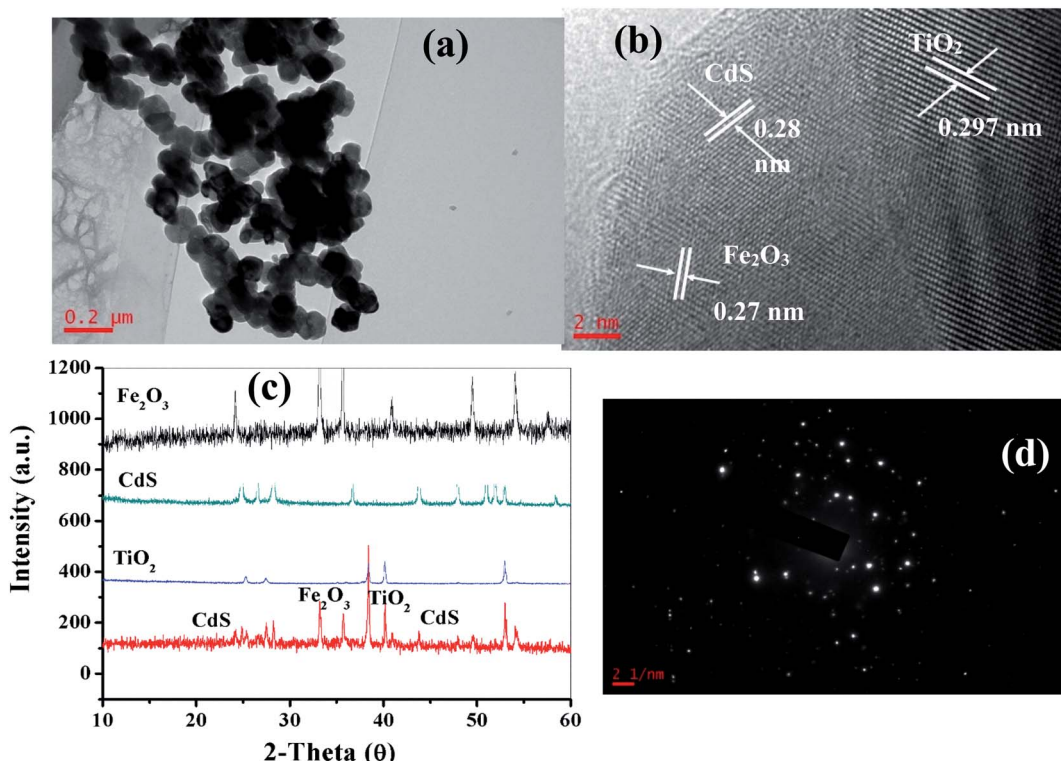


Fig. 3 TEM (a) and HRTEM images (b), XRD patterns (c) and SAED pattern (d) of the as-synthesized CdS/Fe₂O₃/TiO₂ composites.

316 nm, analysed using a UV-vis spectrophotometer (CARY 300 Conc), was used to monitor the photocatalytic degradation. The degradation of the organic pollutant was determined following the Beer-Lambert law for the absorption band with the maximum at 316 nm for PNP. All the measurements were performed at room temperature.

2.4. Analysis of the photodegradation mechanism

Hydroxyl radicals (·OH) produced on the sample surface under AM 1.5G illumination were detected by PL analysis using terephthalic acid (TA), as the probe molecule.^{23,24} Experimental steps were

performed in 5×10^{-4} mol L⁻¹ TA and 2×10^{-3} mol L⁻¹ NaOH solutions. The change of ·OH concentration during the procedure was monitored by determining the fluorescence emission intensity with an excitation wavelength of 320 nm.

3. Results and discussion

3.1. Characterization of the TiO₂/Fe₂O₃/CdS

Fig. 2 shows the SEM images of TiO₂ with/without the deposition of Fe₂O₃ and CdS. As shown in Fig. 2b and c, the surface of the TiO₂ NTAs is homogeneously covered with Fe₂O₃ and CdS nanoparticles. Fig. 2d displays the cross-sectional images of

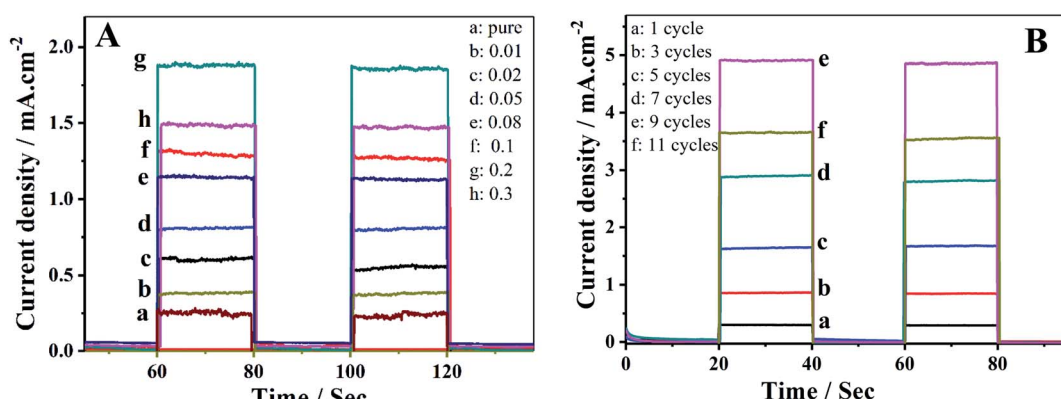


Fig. 4 (A) Photocurrent responses in light on-off process of (a) unmodified TiO₂ nanotubes and (b–h) TiO₂/Fe₂O₃ nanotubes with increasing Fe content. (B) Short-circuit photocurrent density versus time plotted (0 V versus SCE) for TiO₂/Fe₂O₃/CdS with different cycles of CdS.

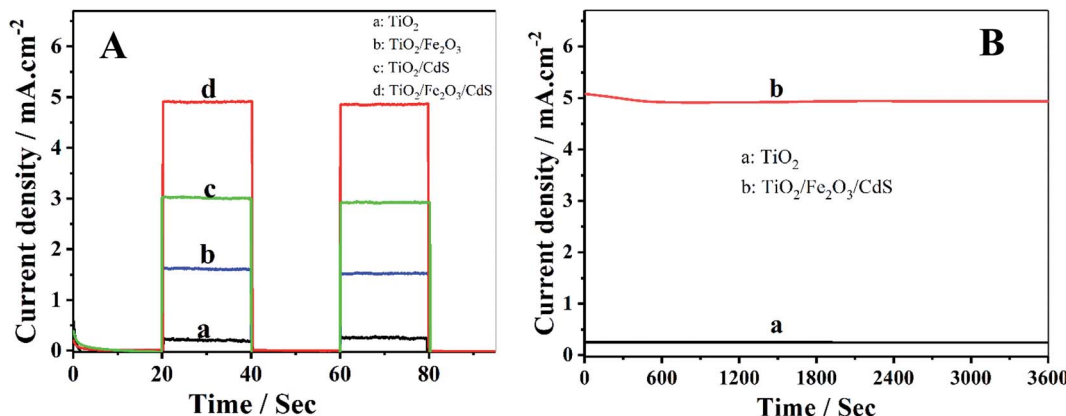


Fig. 5 (A) Photocurrent responses of (a) TiO₂, (b) TiO₂/Fe₂O₃, (c) TiO₂/CdS and (d) TiO₂/Fe₂O₃/CdS; (B) time-dependent photocurrent response of (a) unmodified TiO₂ and (b) TiO₂/Fe₂O₃/CdS.

TiO₂/Fe₂O₃/CdS. The bare TiO₂ NTAs are smooth and clean (Fig. 2a). The Fe₂O₃ nanoparticles are distributed mainly on the top surface and interstices of the NTAs (Fig. 2b). After 9 cycles of CdS adsorption onto the TiO₂/Fe₂O₃ heterostructure, the surface of the material (Fig. 2c and e) becomes a little rougher than undecorated TiO₂/Fe₂O₃ (Fig. 2b), and the gap between TiO₂ NTAs almost disappears owing to the filling of Fe₂O₃ and CdS nanoparticles. No obvious blocking of the entrances is observed and the porosity of the structure is more beneficial for the adsorption process.²⁵ Fig. 2f shows the EDS of the TiO₂/Fe₂O₃/CdS. EDS analysis confirms the successful attachment of the CdS and Fe₂O₃.

As depicted in the TEM image in Fig. 3a, it was observed that the TiO₂/Fe₂O₃/CdS product is composed of many aggregated nanocrystals. The detailed microscopic characterization of the TiO₂/Fe₂O₃/CdS heterostructure is performed using HRTEM images as displayed in Fig. 3b. The measured lattice spacings are consistent with the *d*-spacings of TiO₂ (0.297 nm, JCPDS 21-1272), CdS (0.28 nm, JCPDS 80-0019) and Fe₂O₃ (0.27 nm, JCPDS 72-469), respectively.^{7,26} The nanocrystalline material structure is confirmed with XRD analysis (Fig. 3c) and the SAED pattern (Fig. 3d) which further indicates the presence of TiO₂, Fe₂O₃ and CdS.

3.2. Optimization of the TiO₂/Fe₂O₃/CdS

Fe₂O₃ nanoparticles were firstly immobilized on TiO₂ NTAs by immersing the TiO₂ in FeCl₃ solution from 0.01 mol L⁻¹ to 0.3 mol L⁻¹. Fig. 4A indicates that the photocurrent response varies with Fe content, and the maximum photocurrent (1.89 mA cm⁻², curve g) is obtained on the TiO₂/Fe₂O₃ NTAs with 0.2 mol L⁻¹ Fe, which is 7.56 times that achieved on pure TiO₂ NTAs (0.25 mA cm⁻², curve a).

Further immobilization of CdS nanoparticles on the TiO₂/Fe₂O₃ NTAs resulted in a dramatic increase of the photocurrent up to 4.92 mA cm⁻² by 9 SILAR cycles (Fig. 4B, curve e). The photocurrent density increases first and then decreases (curve f) with increasing CdS loading on the electrodes. Over-loading of CdS nanoparticles beyond 9 SILAR cycles formed a significant aggregation, which is less efficient in absorption spectra as compared to un-aggregated smaller size nanocrystallites, resulting in a decrease in photocurrent.²⁷

3.3. Photoelectrochemical behavior evaluation

Photocurrent density-time characteristics of the samples were investigated in an electrolyte containing 0.35 mol L⁻¹ Na₂SO₃

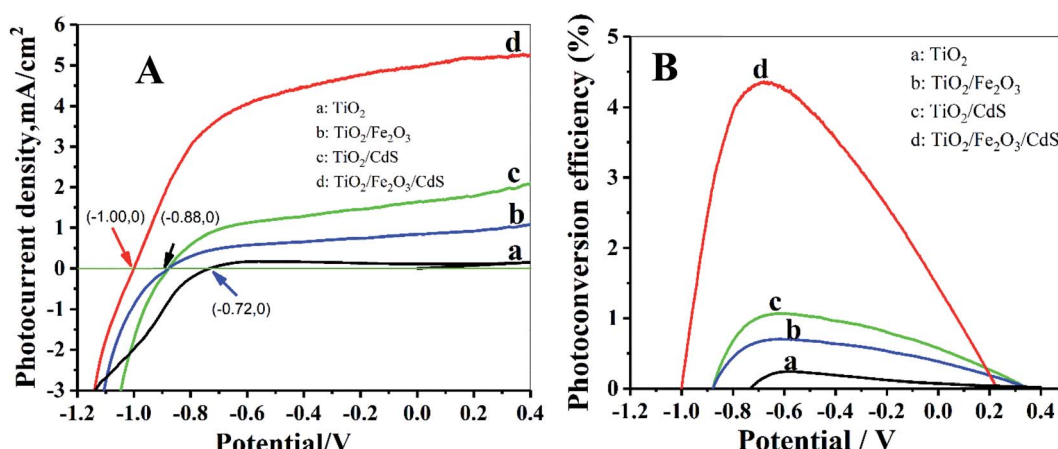


Fig. 6 (A) J-V curves of photoelectrodes; (B) corresponding photoconversion efficiency.



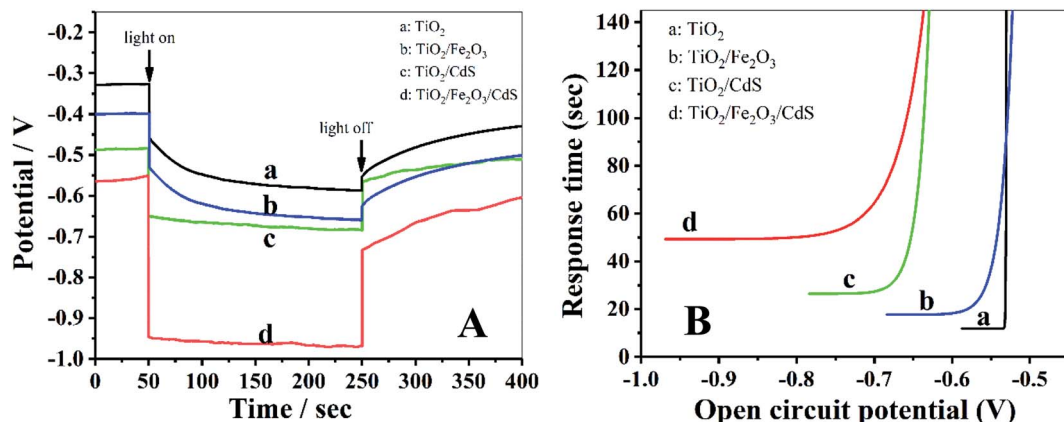


Fig. 7 (A) The open-circuit photovoltage responses of photoelectrodes. (B) Response time determined by open circuit potential decay for the corresponding photoelectrodes shown in (A).

and 0.24 mol L⁻¹ Na₂S to examine the photoelectrochemical properties. The TiO₂/Fe₂O₃/CdS NTAs show the best performances with a photocurrent density of 4.92 mA cm⁻² (curve d) which is much higher than those of the pure TiO₂ (0.25 mA cm⁻², curve a), TiO₂/Fe₂O₃ (1.89 mA cm⁻², curve b) and TiO₂/CdS (3.02 mA cm⁻², curve c) (see Fig. 5A). Fig. 5B shows the time-dependent photocurrent responses of the TiO₂/Fe₂O₃/CdS and unmodified TiO₂ NTAs under illumination with 100 mW cm⁻² visible light. Both show a high stability, and the photocurrent decreases by 1.04% within 1 h.

The photoelectric performance of the TiO₂/Fe₂O₃/CdS is further investigated by the photocurrent–applied potential (*J*–*V*) relationship. As illustrated in Fig. 6A, the photocurrent response increases significantly on the TiO₂/Fe₂O₃/CdS, even at a potential of 0 V. The open circuit potential, *V*_{oc}, which corresponds to the difference between the apparent Fermi levels of the working electrode and the reference electrode, is around -1.00 V for the TiO₂/Fe₂O₃/CdS, which is greater than that obtained with TiO₂/Fe₂O₃ and TiO₂/CdS (*V*_{oc} ≈ -0.88 V) and pure TiO₂ NTAs (*V*_{oc} ≈ -0.72 V), demonstrating a shift in the Fermi level to a more negative potential in the TiO₂/Fe₂O₃/CdS composite system, which can improve the photogenerated electron–hole separation and suppress the recombination of photogenerated charge carriers.²⁸ Fig. 6B displays the corresponding photoconversion efficiency calculated using eqn (1):²⁶

$$\eta (\%) = j_p [E_{\text{rev}}^q - |E_{\text{app}}|] \times 100 / (I_0) \quad (1)$$

where *j*_p is the photocurrent density (mA cm⁻²), *j*_p*E*_{rev}^q is the total power output, *j*_p*|E*_{app}| is the power input, and *I*₀ is the power density of incident light (100 mW cm⁻²). *E*_{rev}^q equals 1.23 V, which is the standard potential for the water splitting reaction. The applied potential is *E*_{app} = *E*_{meas} - *E*_{oc}, where *E*_{meas} is the electrode potential (vs. SCE) of the working electrode and *E*_{oc} is the electrode potential (vs. SCE) of the same working electrode under open-circuit conditions. As expected, the TiO₂/Fe₂O₃/CdS photoelectrode achieves the highest efficiency of 4.36% at -0.68 V vs. SCE which is about 20 times the efficiency of pure TiO₂ (0.22%) as shown in Fig. 6B.

The open-circuit voltage-decay measurements were conducted by monitoring the *V*_{oc} transient during relaxation from an illuminated quasi-equilibrium state to the dark equilibrium,

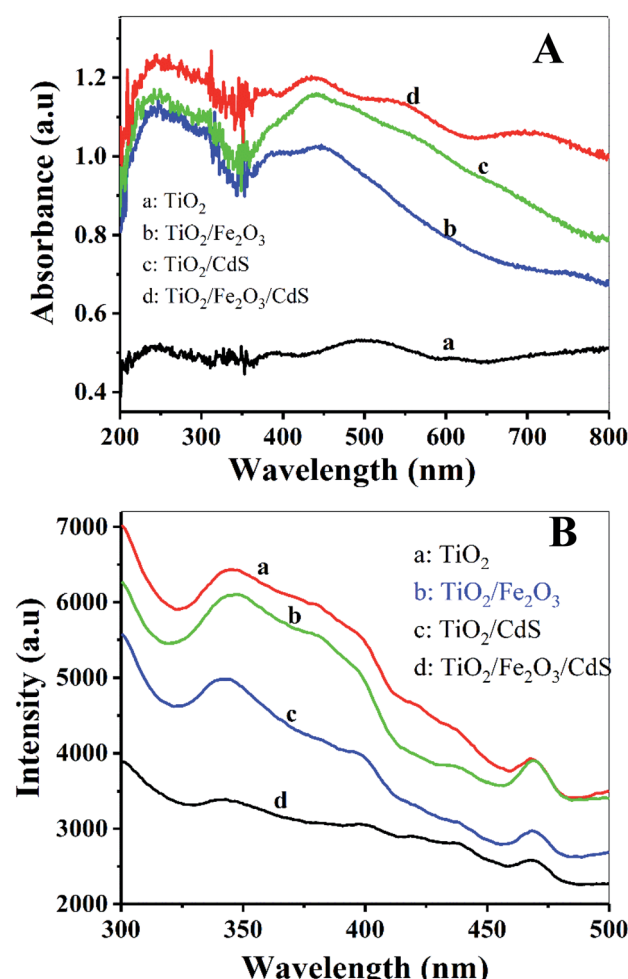


Fig. 8 (A) Diffuse reflectance absorption spectra of (a) TiO₂ NTAs; (b) TiO₂/Fe₂O₃; (c) TiO₂/CdS and (d) TiO₂/Fe₂O₃/CdS. (B) PL spectra of these electrodes.

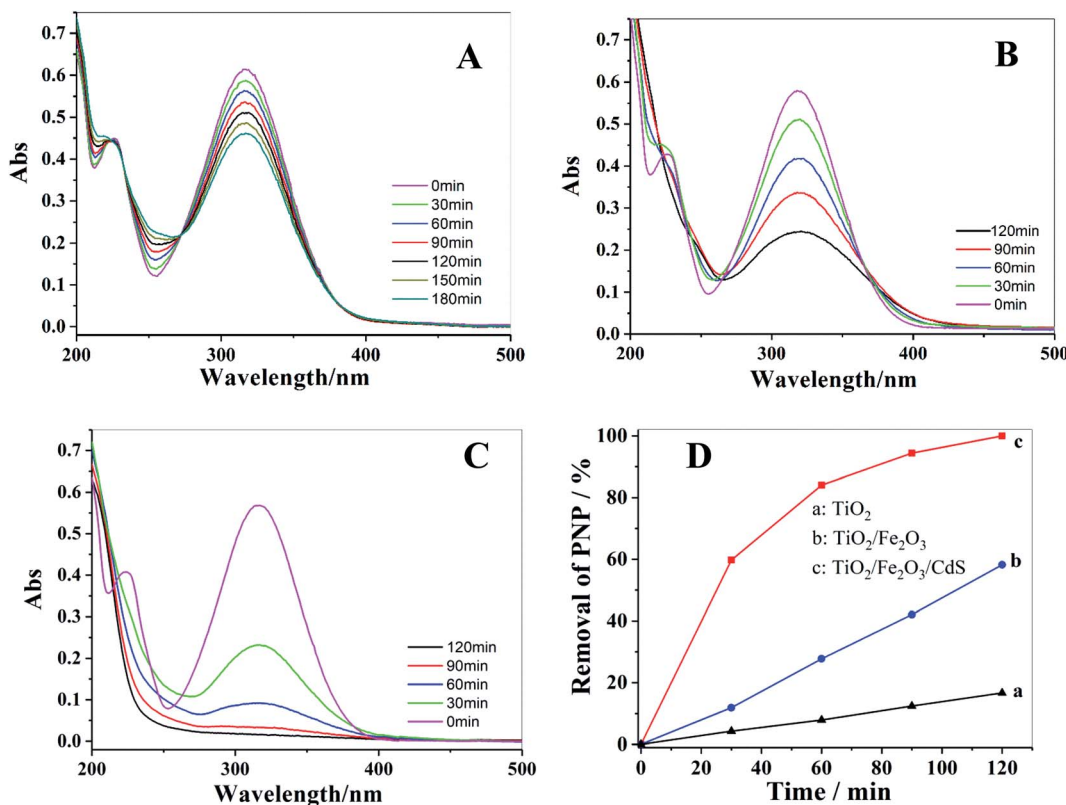


Fig. 9 UV-vis spectra of photocatalytic degradation of PNP with different photoelectrodes: (A) TiO_2 NTAs; (B) $\text{TiO}_2/\text{Fe}_2\text{O}_3$; (C) $\text{TiO}_2/\text{Fe}_2\text{O}_3/\text{CdS}$ and corresponding photocatalytic performances of these electrodes (D).

see Fig. 7A. When the AM 1.5G illumination on the $\text{TiO}_2/\text{Fe}_2\text{O}_3/\text{CdS}$ photoelectrode at open circuit is interrupted, the excess electrons are removed due to recombination with holes trapped in the composite and dissolved oxygen in the electrolyte. The photo-voltage decay rate directly relates to the electron lifetime by expression (2):²⁶

$$\tau_n = \left[\frac{-k_B T}{e} \right] \left[\frac{dV_{oc}}{dt} \right]^{-1} \quad (2)$$

where $k_B T$ is the thermal energy, e is the positive elementary charge, and dV_{oc}/dt is the derivative of the open-circuit voltage transient. Fig. 7B is the plot of the response time obtained by applying eqn (2) to the data in Fig. 7A. At the same V_{oc} value, the response time of the photoelectrodes follows an order of $\text{TiO}_2/\text{Fe}_2\text{O}_3/\text{CdS} > \text{TiO}_2/\text{Fe}_2\text{O}_3 > \text{TiO}_2$ NTAs. Based on the above analyses, the $\text{TiO}_2/\text{Fe}_2\text{O}_3/\text{CdS}$ NTA photoelectrode exhibits superior recombination characteristics, with the longer lifetimes indicating enhanced separation of the photogenerated charges in the structure.

The optical properties of the samples were characterized using the UV-vis diffuse reflectance spectra and PL spectra. Fig. 8A shows that the absorption in the visible range was significantly enhanced with the stepwise modifications of Fe_2O_3 and CdS nanoparticles (curves b and d). Fig. 8B displays a decrease in PL intensity. The photoluminescence is the result of the recombination of photogenerated electrons and holes.¹⁴ Lower photoluminescence intensity represents a lower

recombination rate of photogenerated electron–hole pairs, and consequently a longer lifetime of photogenerated carriers, which implies higher photoelectric conversion efficiency.²⁸ The $\text{TiO}_2/\text{Fe}_2\text{O}_3/\text{CdS}$ NTAs achieve the highest photoelectric conversion efficiency (Fig. 6B), which is consistent with their highest absorbance in visible light.

3.4. Photocatalytic performance and mechanism of the $\text{TiO}_2/\text{Fe}_2\text{O}_3/\text{CdS}$

Photocatalytic degradation of PNP solution under visible light was performed to investigate the photocatalytic activities of TiO_2 NTAs (Fig. 9A), $\text{TiO}_2/\text{Fe}_2\text{O}_3$ (Fig. 9B) and $\text{TiO}_2/\text{Fe}_2\text{O}_3/\text{CdS}$ (Fig. 9C). The change in PNP concentration during the degradation process was characterized following the Beer–Lambert law by its characteristic absorption at 316 nm. After 120 min of illumination, the photocatalytic degradation of PNP on $\text{TiO}_2/\text{Fe}_2\text{O}_3/\text{CdS}$ shows the maximum efficiency; 100% removal is achieved (Fig. 9C), while only 17% and 57.8% removals are achieved on pure TiO_2 NTAs and $\text{TiO}_2/\text{Fe}_2\text{O}_3$ under identical conditions. The removal efficiency is calculated using formula (3):^{29,30}

$$\text{Removal efficiency} = (C_0 - C)/C_0 \times 100\% \quad (3)$$

where C is the PNP concentration obtained after various intervals of time and C_0 is the initial concentration. As shown in Fig. 9D, the $\text{TiO}_2/\text{Fe}_2\text{O}_3/\text{CdS}$ photoelectrode shows the highest



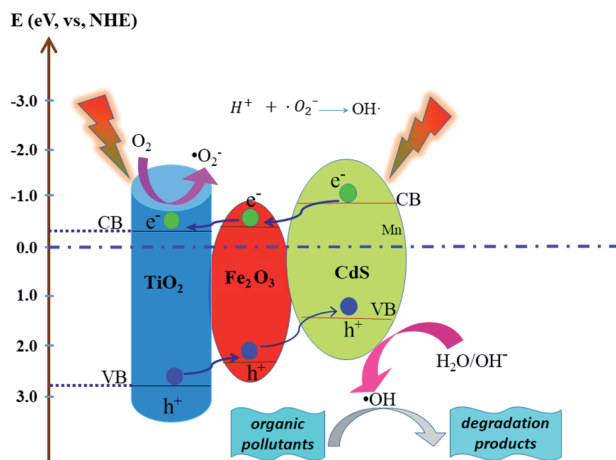
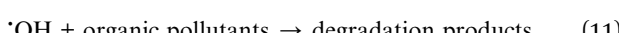
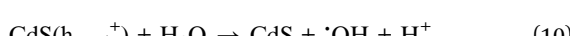
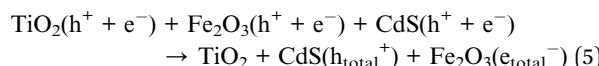
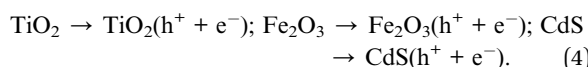


Fig. 10 Schematic mechanism of the possible photogenerated charge separation and transport in the $\text{TiO}_2/\text{Fe}_2\text{O}_3/\text{CdS}$ heterostructure.

activity. Based on previous reports and the results mentioned above, we hypothesize the following photocatalytic degradation mechanism as illustrated in Fig. 10 with the following equations:^{30–34}



Electron–hole pairs are produced in the Fe_2O_3 , CdS and TiO_2 (eqn (4)) under illumination. The band gap of TiO_2 (3.2 eV), CdS (2.4 eV) and Fe_2O_3 (2.2 eV) reduces progressively with the CB and VB increasing progressively to form a step-wise heterostructure that can absorb visible light. The potentials of the conduction band (CB) and valence band (VB) edges of TiO_2 , CdS and Fe_2O_3 were determined using the following formulas:

$$E_{\text{VB}} = X - E_0 + 0.5E_g \quad (12)$$

$$E_{\text{CB}} = E_{\text{VB}} - E_g \quad (13)$$

where E_{VB} and E_{CB} are the VB and CB edge potentials and X is the electronegativity of the semiconductor; the X values for TiO_2 , Fe_2O_3 and CdS are 5.81 eV, 4.78 eV and 5.18 eV, respectively. E_0 is a constant, about 4.5 eV. According to the formulas, the VB and CB values of CdS are calculated to be 1.45 and -0.89 eV, those of TiO_2 are 2.90 and -0.30 eV, and those of Fe_2O_3 are determined to be 2.54 and -0.35 eV, respectively.³⁵ Photo-excited electrons in the CB of CdS transfer to Fe_2O_3 , and then migrate to TiO_2 . On the contrary, the holes in the VB of TiO_2 are transferred to the VB of Fe_2O_3 and CdS stage by stage and eventually accumulate on the surface of CdS (eqn (5)).^{35–39} The separated electrons and the holes are captured by dissolved oxygen molecules and H_2O species respectively to form hydroxyl radicals ($\cdot\text{OH}$) (eqn (6)–(10)), a strong oxidizing agent to decompose organic pollutants (eqn (11)).^{24,40}

The PL technique was employed to help understand the degradation mechanism.⁴¹ TA and $\cdot\text{OH}$ formed on the photo-electrode surface under UV-vis irradiation readily react to produce a highly fluorescent product, 2-hydroxyterephthalic acid.⁴² When the $\text{TiO}_2/\text{Fe}_2\text{O}_3/\text{CdS}$ serves as the photoelectrode, the PL intensity increases gradually with the increasing irradiation time, indicating that $\cdot\text{OH}$ was produced indeed during the photocatalytic process (depicted in Fig. 11A). Fig. 11B shows the PL obtained after 20 min of irradiation for different photo-electrodes, and the $\text{TiO}_2/\text{Fe}_2\text{O}_3/\text{CdS}$ (curve c) shows the best photocatalytic performance.

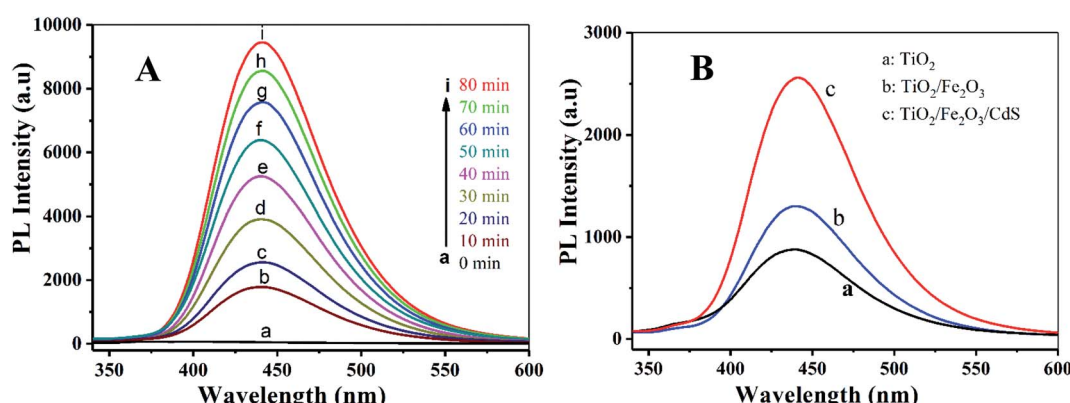


Fig. 11 (A) PL spectra measured during illumination of $\text{TiO}_2/\text{Fe}_2\text{O}_3/\text{CdS}$ and different photoelectrodes (B): (a) TiO_2 , (b) $\text{TiO}_2/\text{Fe}_2\text{O}_3$ and (c) $\text{TiO}_2/\text{Fe}_2\text{O}_3/\text{CdS}$.



4. Conclusions

A $\text{TiO}_2/\text{Fe}_2\text{O}_3/\text{CdS}$ heterostructure was prepared for the first time *via* annealing amorphous TiO_2 NTAs which were pre-loaded with Fe(OH)_3 by S-CBD and SILAR processes. The modification of TiO_2 NTAs with Fe_2O_3 and CdS results in a negative shift of the zero-current potential from -0.72 , -0.88 to -1.0 V, and a significant increase in photocurrent. The optimal sample demonstrates a solar spectrum photoconversion efficiency of approximately 4.36% and an excellent photocatalytic activity for the removal of PNP. A photodegradation mechanism was proposed on the basis of the matched energy band of $\text{TiO}_2/\text{Fe}_2\text{O}_3/\text{CdS}$ favoring the charge transfer and suppressing the photo-induced carrier recombination, leading to the enhanced photocatalytic activity. We believe that it is promising towards the low cost synthesis of high performance photocatalysts for the photodegradation of organic pollutants in aqueous solution.

Conflicts of interest

The authors declare no competing financial interest.

Acknowledgements

This work was financially supported by the National Science Foundation of China (Grant No. 21175038, 21235002 and 21502051), Natural Science Foundation of Hunan Province (2016JJ6101), and Dr Start-up Foundation (Grant No. 15BSQD14). We thank the editor and reviewers for helpful comments and suggestions.

References

- W. Li, J. Yang, Z. Wu, J. Wang, B. Li, S. Feng, Y. Deng, F. Zhang and D. Zhao, *J. Am. Chem. Soc.*, 2012, **134**, 11864–11867.
- G. Cheng, F. Xu, J. Xiong, Y. Wei, F. J. Stadler and R. Chen, *Adv. Powder Technol.*, 2017, **28**, 665–670.
- X. Lv, J. Deng and X. Sun, *Appl. Surf. Sci.*, 2016, **369**, 314–319.
- X. Yin, P. Sheng, F. Zhong, V. Nguyen, Q. Cai and C. Grimes, *New J. Chem.*, 2016, **40**, 6675–6685.
- S. Kuang, L. Yang, S. Luo and Q. Cai, *Appl. Surf. Sci.*, 2009, **255**, 7385–7388.
- H. B. Yang, J. Miao, S.-F. Hung, F. Huo, H. M. Chen and B. Liu, *ACS Nano*, 2014, **8**, 10403–10413.
- H. Yao, L. Liu, W. Fu, H. Yang and Y. Shi, *FlatChem*, 2017, **3**, 1–7.
- S. J. A. Moniz, S. A. Shevelin, X. An, Z.-X. Guo and J. Tang, *Chem-Eur. J.*, 2014, **20**, 15571–15579.
- Y. Xia and L. Yin, *Phys. Chem. Chem. Phys.*, 2013, **15**, 18627–18634.
- Q. Sun, W. Leng, Z. Li and Y. Xu, *J. Hazard. Mater.*, 2012, **229–230**, 224–232.
- X. Cao, S. Luo, C. Liu and J. Chen, *Adv. Powder Technol.*, 2017, **28**, 993–999.
- W. Li, P. Sheng, H. Feng, X. Yin, X. Zhu, X. Yang and Q. Cai, *ACS Appl. Mater. Interfaces*, 2014, **6**, 12353–12362.
- H. Feng, W. Zhou, X. Zhang, S. Zhang, B. Liu and D. Zhen, *Adv. Compos. Lett.*, 2019, **28**, 1–10.
- L. Wang, W. Gu, P. Sheng, Z. Zhang, B. Zhang and Q. Cai, *Sens. Actuators, B*, 2019, **281**, 1088–1096.
- M. Altomare, N. T. Nguyen, S. Hejazi and P. Schmuki, *Adv. Funct. Mater.*, 2018, **28**, 1704259.
- L. Cheng, Q. Xiang, Y. Liao and H. Zhang, *Energy Environ. Sci.*, 2018, **11**, 1362–1391.
- X. Ning and G. Lu, *Nanoscale*, 2020, **12**, 1213–1223.
- S. G. Kumar, R. Kavitha and P. M. Nithya, *J. Environ. Chem. Eng.*, 2020, **8**, 104313.
- R. Yin, M. Liu, R. Tang and L. Yin, *Nanoscale Res. Lett.*, 2017, **12**, 520.
- G. Larramona, C. Choné, A. Jacob, D. Sakakura, B. Delatouche, D. Pérez, X. Cieren, M. Nagino and R. Bayón, *Chem. Mater.*, 2006, **18**, 1688–1696.
- H. Feng, S. Zhang, X. Zhang, B. Liu and N. Tang, *Anal. Methods*, 2018, **10**, 3462–3469.
- F. Sastre, A. V. Puga, L. Liu, A. Corma and H. García, *J. Am. Chem. Soc.*, 2014, **136**, 6798–6801.
- S. Khanchandani, S. Kundu, A. Patra and A. K. Ganguli, *J. Phys. Chem. C*, 2012, **116**, 23653–23662.
- Z. Wu, X. Tong, P. Sheng, W. Li, X. Yin, J. Zou and Q. Cai, *Appl. Surf. Sci.*, 2015, **351**, 309–315.
- J. Fu, Y. Tian, B. Chang, F. Xi and X. Dong, *J. Mater. Chem.*, 2012, **22**, 21159–21166.
- H. Feng, N. Tang, S. Zhang, B. Liu and Q. Cai, *J. Colloid Interface Sci.*, 2017, **486**, 58–66.
- H. Feng, T. Tran T., L. Chen, L. Yuan and Q. Cai, *Chem. Eng. J.*, 2013, **215–216**, 591–599.
- Q. Kang, Q. Z. Lu, S. H. Liu, L. X. Yang, L. F. Wen, S. L. Luo and Q. Y. Cai, *Biomaterials*, 2010, **31**, 3317–3326.
- H. Zhang, L. Zhao, F. Geng, L.-H. Guo, B. Wan and Y. Yang, *Appl. Catal., B*, 2016, **180**, 656–662.
- W. Li, L. Yao, Z. Zhang, H. Geng, C. Li, Y. Yu, P. Sheng and S. Li, *Mater. Sci. Semicond. Process.*, 2019, **99**, 106–113.
- D. Liu, Z. Zheng, C. Wang, Y. Yin, S. Liu, B. Yang and Z. Jiang, *J. Phys. Chem. C*, 2013, **117**, 26529–26537.
- M. A. Mahadik, P. S. Shinde, M. Cho and J. S. Jang, *J. Mater. Chem. A*, 2015, **3**, 23597–23606.
- X.-F. Gao, H.-B. Li, W.-T. Sun, Q. Chen, F.-Q. Tang and L.-M. Peng, *J. Phys. Chem. C*, 2009, **113**, 7531–7535.
- H. Zhang, X. Quan, S. Chen, H. Yu and N. Ma, *Chem. Mater.*, 2009, **21**, 3090–3095.
- R. Lei, H. Ni, R. Chen, H. Gu, B. Zhang and W. Zhan, *J. Colloid Interface Sci.*, 2018, **514**, 496–506.
- M. Tong, D. Sun, R. Zhang, H. Liu and R. Chen, *J. Alloys Compd.*, 2021, **862**, 158271.
- S. Zhang, W. Xu, M. Zeng, J. Li, J. Xu and X. Wang, *Dalton Trans.*, 2013, **42**, 13417–13424.
- P. Kuang, L. Zhang, B. Cheng and J. Yu, *Appl. Catal., B*, 2017, **218**, 570–580.
- Y.-S. Lee, C. V. V. M. Gopi, A. Eswar Reddy, C. Nagaraju and H.-J. Kim, *New J. Chem.*, 2017, **41**, 1914–1917.
- C.-C. Hu, T.-C. Hsu and S.-Y. Lu, *Appl. Surf. Sci.*, 2013, **280**, 171–178.
- J. Yu, W. Wang, B. Cheng and B.-L. Su, *J. Phys. Chem. C*, 2009, **113**, 6743–6750.
- Q. Xiao, Z. Si, J. Zhang, C. Xiao and X. Tan, *J. Hazard. Mater.*, 2008, **150**, 62–67.

